A Velocity Ambiguity Resolution Algorithm Based on Improved Hypothetical Phase Compensation for TDM-MIMO Radar Traffic Target Imaging

Bo Yang, *Student Member, IEEE*, Siqi Liu, *Student Member, IEEE*, Hua Zhang, and Yongjun Zhou

***Abstract*—In principle, the imaging millimeter-wave radar based on time-division multiplexing multiple-input multiple-output (MIMO) technologies can provide richer target information for intelligent transportation systems due to the high-density target point cloud output. However, the chirp repetition interval extension reduces radar's inherent maximum detectable velocity, leading to the unavoidable problem of estimating the target velocity with a large ambiguity period in imaging radar moving target surveillance applications. To alleviate these problems, we propose an improved hypothetical phase compensation algorithm. Unlike the original method of determining the Doppler ambiguity period by comparing the peak amplitude of the angular power spectrum in each hypothetical case, the proposed algorithm selects the peak of the angular power signal-to-noise ratio (SNR) spectrum as the processing object and jointly decides the target speed by the average of the two highest wave peak intervals in the SNR variation curve. Simulations and practical experiments show that the improved algorithm has higher anti-interference performance. In particular, the proposed algorithm can remain continuously effective when multiple targets or angle information exist in the same distance Doppler cell, making it more suitable for MIMO imaging applications.**

***Index Terms*—Hypothetical phase compensation (HPC), millimeter-wave radar, time-division multiplexing multiple input multiple output (TDM-MIMO), velocity ambiguity resolution.**

I. Introduction

MILLIMETER-WAVE radar has been used in urban traffic applications due to its high environmental resistance and high speed, distance, and angle measurement accuracy characteristics [1]. For example, traffic detection radar based on phased array modulation is used to implement traffic flow [2], speed [3], and traffic event detection. With the application and development of multiple-input multiple-output (MIMO) technology, millimeter-wave radar achieves virtual aperture expansion to obtain higher angular resolution by modulating the emission method (e.g., time-division multiplexing (TDM) [4], frequency-division multiplexing [5], and code-division multiplexing [6]) without increasing the number of antennas, which gives MIMO radar the capability of target point cloud imaging and environmental awareness. For example, the MIMO radar point cloud image is utilized to implement sensing of the surrounding environment of vehicle bodies [7], [8], road curvature estimation [9], and road surface classification [10].

Theoretically, road monitoring using MIMO radar can provide richer and more realistic traffic target information for intelligent transportation systems, such as additional information on vehicle height, profile, and type [7], [11], [12]. However, the extended chirp repetition interval makes the maximum unambiguous speed of the MIMO radar just $1/M$ times that of the phased array radar, where M is the actual number of transmitting antennas (TXs). The need for distance in surveillance missions also leads to a further reduction in the maximum unambiguous speed of the radar. For an MIMO radar system, a vehicle traveling at normal speed on an urban road may produce more than two times the speed ambiguity period. Unfortunately, incorrect target velocity estimation in MIMO radar systems will affect the accuracy of target angle estimation due to the coupling between velocity and angle. Therefore, decoupling velocity ambiguity is one of the crucial techniques for MIMO imaging radar in traffic surveillance applications.

Resolving Doppler ambiguity is a challenging problem. Utilizing the multi-pulse-repetition-frequency (PRF) scheme is the most commonly used method, including the Chinese remainder theorem [13], the 1-D set algorithm [14], the lookup table method algorithm [15], and the multifrequency observation algorithm [16]. Taking a typical Chinese residual theorem (CRT) algorithm as an example, the radar alternately transmits two frame signals with different chirp periods so that the same target is estimated to have different velocities in different transmitted waveforms, and then, the target velocity ambiguity cycle is obtained by solving for the maximum common divisor between the two speeds. In addition, several improved algorithms have been proposed to increase the robustness of the CRT algorithm, including optimizing the remaining PRF by constraining the minimum sidelobes of the maximum likelihood criterion [17], proposing a phase unwrapping algorithm to reduce the effect of

Manuscript received 6 September 2023; revised 9 November 2023 and 20 December 2023; accepted 6 January 2024. Date of publication 10 January 2024; date of current version 23 January 2024. This work was supported in part by the Technology on Near-Surface Detection Laboratory under Grant 6142414211202, in part by the Civil Aerospace Technology Advanced Research Project under Grant D020403, and in part by the Basic Research Project under Grant 50236170112202. *(Corresponding author: Hua Zhang.)*

Bo Yang, Siqi Liu, and Hua Zhang are with the School of Aerospace Science and Technology, Xidian University, Xi'an 710071, China (e-mail: byang_18@stu.xidian.edu.cn; 21131213377@stu.xidian.edu.cn; zhanghua@mail.xidian.edu.cn).

Yongjun Zhou is with the Science and Technology on Near-Surface Detection Laboratory, Wuxi 214035, China (e-mail: zhouyongjun_bj@163.com).

Digital Object Identifier 10.1109/JSTARS.2024.3352082

the residual error on the integer solution [18], and presenting the closed-form robust CRT to reduce algorithm complexity [19]. However, the need for at least two sets of frequency-modulated continuous-wave signals makes the radar system less real time, and the matching between targets in multitarget scenarios increases the complexity and error of the algorithm [20].

To alleviate the above problems, some single-frame velocity deambiguity schemes have been proposed. In [21], a resolution scheme via exploiting carrier frequency multiplexing is proposed. However, the method only requires a set of primary linear frequency-modulated continuous-wave (LFMCW) signals but increases the signal bandwidth, which puts higher demands on the radar analog-to-digital converter sampling rate. To avoid the modification of the radar transmit waveform, literature [22] utilizes overlapping elements in the antenna array to achieve the Doppler ambiguity period solution, but it also limits the antenna array layout. In addition, some researchers have utilized nonlinear phase components of the linear frequency-modulated signal echo to resolve this ambiguous estimation [23], but it also increases the computational effort.

In [24] and [25], the hypothetical phase compensation (HPC) algorithm was proposed based on the relationship between the velocity-induced Doppler phase and the peak of the target angular power spectrum, i.e., the more accurate the Doppler phase compensation is, the higher the peak of the criterion angular power spectrum. Theoretically, in addition to the low-latency characteristics common to single-frame velocity ambiguity resolution scheme, the HPC algorithm increases the maximum estimated speed of the radar system by M_{TX} (transmitter antenna number) times via searching for the hypothetical case where the peak of the target angular power spectrum is the largest among all the Doppler phase compensation assumptions, which makes it more suitable for dynamic scenarios of urban vehicle surveillance.

Although the HPC algorithm is easy to implement, the peak angular power spectrum is highly influenced by noise making the HPC algorithm less stable. In particular, the algorithm fails when there are multiple targets within the same distance Doppler cell, which is detrimental to the implementation of vehicle surveillance via planar or spatial stereo imaging using MIMO radar. Therefore, we propose an improved HPC algorithm and verify its performance through simulation and practical tests. The contributions of this article are summarized as follows.

1) First, we select the highest value of the angular power spectrum signal-to-noise ratio (SNR) in each hypothetical case instead of the peak power to form the SNR variation curve. Compared to the peak power spectrum, the peak of SNR is more stable, which avoids the false detection of spurious peaks due to noise fluctuations or the superposition of multiple target flap energies.
2) Next, a comparison is made between the first and second peaks in the SNR curves. If the first peak is much larger than the second peak, the Doppler phase corresponding to the first peak is considered the actual target phase. Otherwise, the Doppler ambiguity period is judged by the magnitude of the mean value in the waveform interval. Introducing the second spectral peak can effectively prevent the interference of anomalous shock points compared to selecting only the peak value as a decision.
3) Numerical simulations show that the proposed algorithm has higher accuracy and better velocity and angle estimation stability than those of the HPC algorithm. The superiority of the proposed algorithm becomes more significant as the number of targets in the same distance–velocity Doppler cell increases.
4) Two radar physical platforms and real traffic scenarios are demonstrated for performance verification and comparison of the proposed algorithm. The experiments show that the proposed algorithm has a better imaging effect than that of the HPC algorithm in both planar imaging and spatial stereo imaging, and the experimental results are consistent with the simulation results.

The rest of this article is organized as follows. Section II provides a millimeter-wave radar signal model and theoretically analyzes the impact of velocity ambiguity on MIMO radar angle estimation. Sections III and IV elaborate on the improved HPC algorithm model and the unified conditions for algorithm performance verification. Sections V and VI validate and analyze the functionality and performance of the proposed algorithm from both digital simulation and actual scenarios. Finally, Section VII concludes this article.

II. Radar Signal Modeling and Influence of Velocity on Angle

A. Radar Signal Model

In the LFMCW radar system, the radar transmits a sawtooth signal (called chirp) through the TX, which can be expressed as

$$s(t) = \exp\left(j2\pi\left(f_o t + \frac{1}{2}kt^2\right)\right) \tag{1}$$

where f_o is the starting frequency and $k = B/T_c$ is the slope, where B is the bandwidth and T_c is the duration of chirp. Here, we consider the initial phase to be 0 and do not consider energy amplitude changes.

The transmitted signal is received by the radar receiving antenna (RX) after being reflected by the target, and the echo signal can be expressed as

$$s'(t) = \exp\left(j2\pi\left(f_o\left(t-\tau\right) + \frac{1}{2}k\left(t-\tau\right)^2\right)\right) \tag{2}$$

where τ is the electromagnetic wave travel time. The beat frequency signal is obtained when the echo signal is mixed with the transmitted signal, which can be expressed as

$$y = \exp\left(j2\pi(f_o\tau + kt\tau - \frac{1}{2}k\tau^2\right). \tag{3}$$

To obtain the distance and speed of the target, the radar emits multiple chirp signals in one frame processing time. Assuming that the initial distance between a target and the radar is R and the radial velocity is v, the expression for τ is

$$\tau(t) = 2 * \frac{R + vt + v(l-1)T_c}{c} \tag{4}$$

where c is the speed of light, $l = 1, 2, 3, \ldots, L$, and L is the total number of chirp in a data frame. Then, the expression of (4) can be changed to

$$f_b \approx \frac{2kR}{c} + \frac{2vf_o}{c} \tag{5a}$$

$$f_d = \frac{2vf_o}{c} \tag{5b}$$

$$\phi_l = f_d(l-1)T_c + \frac{2f_oR}{c} \tag{5c}$$

$$y(l) = \exp(j2\pi(f_b)t)\exp(j2\pi\phi_l) \tag{5d}$$

where f_b denotes the frequency of the beat signal, which is related to the distance of the target (assuming that the displacement of the target in one frame time is ignored), ϕ_l denotes the phase of the lth echo, which is related to the speed of the target, and f_d denotes Doppler.

Then, expression (6) can be approximated by the two-dimensional fast Fourier transform (2-D FFT)

$$S = \int_0^{LT_c} \int_\tau^{T_c} \exp\left(j2\pi\left(f_1 - f_b\right)t_1\right) dt_1 \\ *\exp\left(j2\pi\left(f_2 - f_d\right)t_2\right) dt_2. \tag{6}$$

Obviously, the signal power is maximum when $f_1 = f_d$ and $f_2 = f_b$. Therefore, in practical engineering applications, the 2-D FFT is used to obtain the range–Doppler power spectral matrix (RDM), and the RDM is fed into the constant false alarm detector to obtain frequency points (f_b and f_d) related to the target distance and velocity.

B. TDM-MIMO Model

In a radar system, at least two or more RXs are required to estimate the target angle information. In the TDM-MIMO mode, the radar realizes the RX aperture expansion using time-sharing signal transmission at the transmitter side, and its effect is consistent with the result of increasing physical antennas. When the number of TXs and RXs of the radar system is M_{TX} and N_{RX}, respectively, the maximum virtualizable number is $M_{\text{TX}} * N_{\text{RX}}$.

For the convenience of description, we assume that there are M TXs and one RX and illustrate the TDM-MIMO mode of operation in Fig. 1. Each TX sequentially transmits a chirp signal and is received by the antenna, and M RDMs are obtained through data separation, recombination, and 2-D FFT operations.

There is a phase difference (Φ) in the signal between the receiving channels due to different positions of the receiving channels. Assuming RX1 and TX1 as reference antennas, the signal expression received by each channel is

$$Y_m = S * \exp\left(j2\pi\Phi_m\right) = S * \exp\left(j2\pi d_m \sin\theta/\lambda\right) \tag{7}$$

where d_m represents the position between the mth antenna and the reference antenna, $m = 1, 2, \ldots, M$, and $d_1 = 0$. Obviously, with the same range–Doppler unit, there is only a one-phase difference between the signals received from different channels due to different antenna positions.

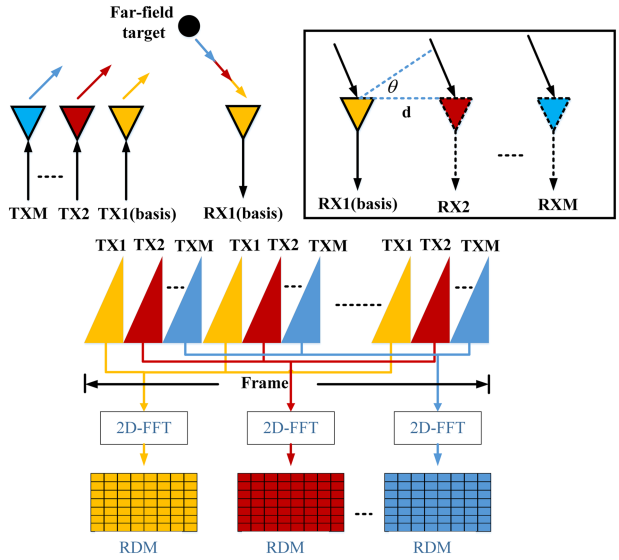

Fig. 1. TDM-MIMO model.

The target angle can be obtained by processing the phase difference between the channels utilizing 3-D FFT (uniform line array) or digital beam synthesis methods.

C. Influence of Velocity on Angle

However, (7) only applies to stationary targets. When there is a velocity on the target, there is also a target Doppler-related phase factor between the signals due to the time difference between the signals emitted by the TX. Then, the signal expression is

$$\varphi = 4\pi v_{\text{target}} M T_c/\lambda \tag{8a}$$

$$Y_m = S * \exp\left(j2\pi\Phi_m\right) * \exp\left(j\frac{\varphi}{M} * (m-1)\right). \tag{8b}$$

Therefore, Doppler phase compensation must be applied to the data from different channels before estimating the target angle.

To more intuitively understand the effect of the target speed when it exceeds the maximum unambiguous speed of the radar, we give the results of a simulation experiment (shown in Fig. 2). Assume that the target speed is V

$$V = V_0 + N * V_{\max} \tag{9}$$

where $V_0 \in [0, V_{\max}]$ and $V_{\max}$ is the radar maximum unambiguous speed in the positive, because positive and negative speeds give the same effect. $N = 1, 2, \ldots, 9$ denotes the multiplier, which represents how many times the current speed exceeds the maximum unambiguous speed of the radar. As N increases (target velocity increases in multiples of $V_{\max}$), the difference between the target velocity detected by constant false alarm rate detector (CFAR) and the actual target velocity keeps growing [as shown in Fig. 2(a)]. At the same time, the radar angle estimation error also increases gradually [as shown in Fig. 2(b)]. In addition, as the angle of the target with respect to the radar center is larger, the error between the value of the estimated angle and the actual angle is larger. Therefore, resolving velocity blur is important

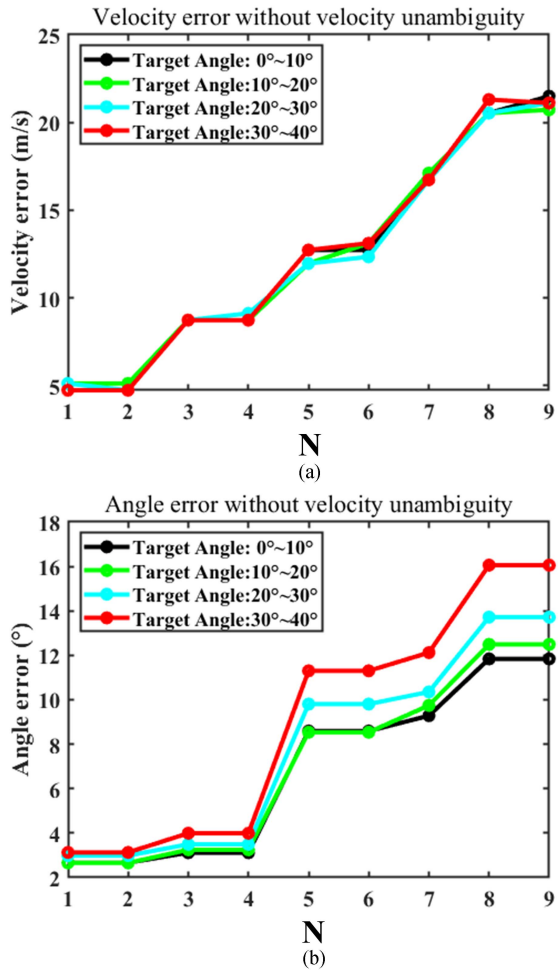

Fig. 2. Effect of target velocity on radar velocity estimation and angle estimation when the target velocity is greater than the maximum unambiguous radar velocity. (a) Relationship between the maximum unambiguous speed multiplier (N) and velocity estimation error. (b) Relationship between the maximum unambiguous speed multiplier (N) and angle estimation error.

for MIMO radar imaging, especially in cases with large blur periods.

III. Improved HPC Algorithm

A. Phase Relationship and the HPC Algorithm Overview

Usually, we use the Doppler phase obtained by the CFAR detector to implement compensation. According to the transmission mode of TDM-MIMO, it represents the phase difference between two transmitted signals from the same TX. However, this only applies to situations where the target velocity is less than the maximum unambiguous velocity of the radar.

We define H_a as a hypothetical case regarding the target velocity, where a represents the value of q, i.e., the Doppler ambiguity period. Fig. 3 shows the relationship between the target true Doppler phase (φ_{true}) and the detection phase (φ_{cfar}) obtained by the CFAR detector with q from -1 to 1 (H_{-1}, H_0, and H_1). The relationship between phases can be expressed as

$$\varphi_{\text{true}} = \varphi_{\text{cfar}} + 2q\pi \tag{10}$$

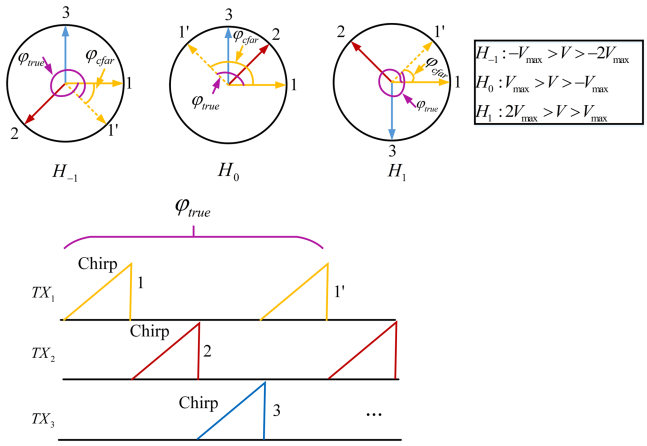

Fig. 3. Three different phase hypotheses for the same detection velocity with three TXs.

where q represents the ambiguity period, $q \in \mathbb{Z}$. Only when the target speed is less than the maximum unambiguous speed, $\varphi_{\text{cfar}} = \varphi_{\text{true}}$; otherwise, there is a phase difference of 2π integer multiples. Assuming that TX_1 is the reference antenna, the phase generated by the other TXs is evenly divided by $2q\pi$

$$\varphi_{\text{true}} - \varphi_{\text{cfar}} = \frac{i}{M}(2q\pi), \quad i \in [1, M_{\text{TX}} - 1]. \tag{11}$$

After compensating only φ_{cfar}, all the channels have individual constant phase shifts, given by (11), which depend on the number of TXs and form unique patterns.

Furthermore, we have expanded the number of antennas to 5, i.e., the compensated phase patterns with q range from -3 to 3 for three different antenna arrays having three, four, and five transmitters are shown in Fig. 4, respectively. In the case of $\text{TX} = 3$, when the target Doppler ambiguity period is not greater than 1 ($|q| <= 1$), the channel phases in each hypothetical case are different from each other ($H_0 \neq H_1 \neq H_{-1}$), i.e., the Doppler phase caused by the target velocity corresponds uniquely to H. When the ambiguity period is greater than 1 ($|q| > 1$), there is a situation where H is the same ($H_2 = H_{-1}, H_{-2} = H_1$), i.e., Doppler phase does not correspond uniquely to H. To eliminate velocity ambiguity, the channel phases between different H must be different from each other. Therefore, the effective value of q is $|q| <= 1$. Similarly, when $\text{TX} = 4$ and $\text{TX} = 5$, the effective range of values for q is $|q| <= 1$ and $|q| <= 2$, respectively. Then, some conclusions can be obtained.

1) As the number of TXs increases, the nonambiguous phase range becomes larger (as shown in the green area in Fig. 4), which means that the range of q values becomes wider.
2) In theory, the relationship between q and the TX is: if M_{TX} is odd, then $|q| <= (M_{\text{TX}} - 1)/2$; otherwise, $|q| <= (M_{\text{TX}}/2) - 1$.

Different H corresponds to different Doppler compensation values; according to (8), the Doppler phase compensation results will also have an impact on the peak of the target angular power spectrum, i.e., the closer the compensated Doppler value is to the true target velocity, the higher the peak of the target angle power spectrum. Based on the amplitude change characteristics,

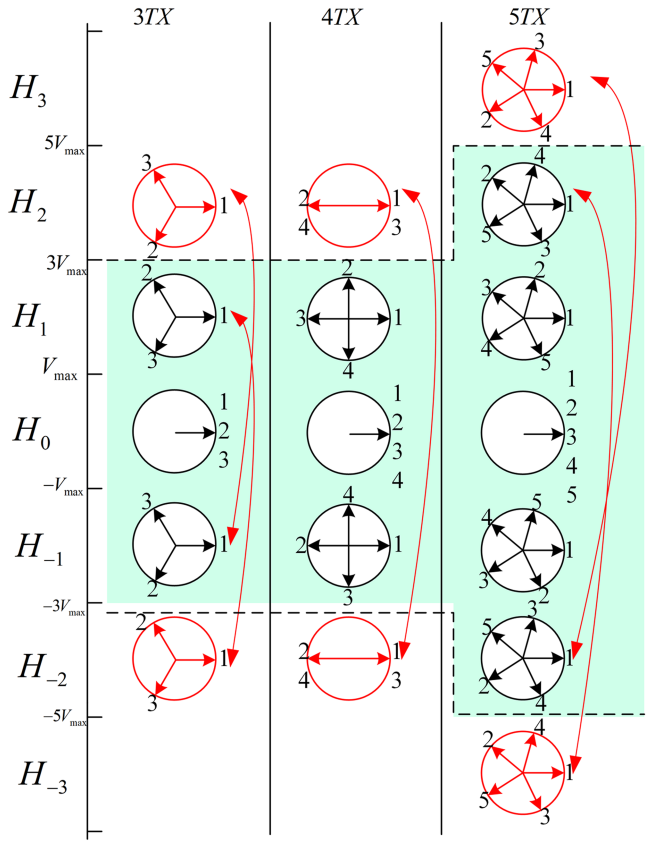

Fig. 4. Compensated phase pattern for three, four, and five transmitters.

the HPC algorithm is proposed. The algorithm principle is: in the nonambiguous interval, the Doppler phase generated by the real target uniquely corresponds to H, and the peak value of the target's angular power spectrum is highest after compensation. Then, the target speed can be obtained by comparing the peak values of the angle power spectrum at each H.

In addition, there is a fixed relationship between the Doppler ambiguity period and the target velocity

$$V_{\text{true}} = V_{\text{cfar}} + 2qV_{\max} \tag{12}$$

where V_{true} represents the true speed of the target, V_{cfar} represents the estimated speed obtained from the detection results of the CFAR detector, and $V_{\max}$ represents radar maximum unambiguous speed. If the speed defuzzification algorithm is not implemented, the maximum detectable speed range of the radar is only $[-V_{\max}, +V_{\max}]$. However, using the HPC algorithm, it is possible to extend the maximum detectable speed of the radar to $[-M_{\text{TX}}V_{\max}, +M_{\text{TX}}V_{\max}]$ (if M_{TX} is odd), which greatly improves the ability of MIMO radar to detect moving targets.

B. Improved HPC Algorithm Model

Although the HPC algorithm can highly expand the speed detection range of MIMO radar systems and is easy to implement in engineering, its stability is poor as the q interval increases due to the susceptibility of power spectrum peaks to noise, interference, and other targets. Especially, when multiple targets are in the same range–Doppler cell, the HPC algorithm has a high probability of failure, which is unfavorable for high-resolution MIMO radar moving target imaging. To alleviate the above issues, we propose an improved HPC algorithm named HPC-SNR (in this article, the original algorithm is called the HPC-Peak).

A complete HPC-SNR model mainly includes the parameter input part, Doppler phase compensation and angle estimation part, angle spectrum (SNR) part, SNR peak value curve part, and decision making (as shown in Fig. 5). Moreover, the processing flow of using the HPC-SNR algorithm to resolve speed ambiguity to obtain the actual velocity and angle of the target is as follows.

Step 1 (Parameter input): Before implementing the algorithm, the detection phase (ϕ_{cfar}), channel dataset $(\boldsymbol{S})$, and hypothetical number (q) need to be determined. Through the CFAR detector, the distance and the Doppler index of the target in the RDM can be obtained, and ϕ_{cfar} can be calculated based on the Doppler index. At the same time, we extract data from the same index position in each channel RDM to form a channel dataset $(\boldsymbol{S} = s_{(1,1)}, s_{(2,1)}, \ldots, s_{(M_{\text{TX}},1)}, s_{(2,1)}, \ldots, s_{(M_{\text{TX}},N_{\text{RX}})})$ for angle estimation. The specific q value can be calculated based on the number of TXs in the radar system.

Step 2 (Doppler phase compensation and angle estimation): First, based on the q value, list all the HPC cases

$$\boldsymbol{H} = H_{-q}, \ldots, H_k, \ldots, H_q. \tag{13}$$

Any H represents a hypothetical case where the compensation phase is (ϕ_{com})

$$\phi_{\text{com}}^k = \phi_{\text{cfar}} + 2k\pi, \quad k = -q, -q+1, \ldots, q. \tag{14}$$

Next, phase compensation is applied to the channel data under each hypothetical scenario

$$\boldsymbol{S^K} = f(\boldsymbol{S}, H_k) \tag{15}$$

$$s_{m,n}^k = s_{m,n} * \exp\left(-j\frac{\phi_{\text{com}}^k}{M_{\text{TX}}} * (m-1)\right) \tag{16}$$

where $f(\boldsymbol{S}, H_k)$ represents the compensation function of channel data S under the H_k hypothesis, and its compensation method is shown in (15). Then, FFT or DBF operations are performed on the compensated channel data (S^k) to obtain the angular power spectrum. Unlike the HPC-Peak algorithm, we convert the angular power spectrum into an SNR spectrum.

Finally, an angle SNR spectrum will be obtained for each H case, with a total of $2q+1$.

Step 3 (SNR peak spectrum mapping and processing): A curve about the change in the magnitude of the SNR amplitude is formed by extracting the maximum value of the angular SNR spectrum in each H in turn, where the horizontal coordinate indicates which H the SNR value belongs to and the vertical coordinate indicates the magnitude of the SNR value. Then, the largest peak value (D_k), the second largest peak value (D_p), and the neighboring values in the curve $(D_{k-1}, D_{k+1}, D_{p-1}$, and $D_{p+1})$ were found by spectral peak search. D_k, D_p, AVE_k, and AVE_p were sent to the decision part, where $SUM_k = (D_{k-1} + D_k + D_{k+1})$, $SUM_p = (D_{p-1} + D_p + D_{p+1})$, and A denotes the mean value.

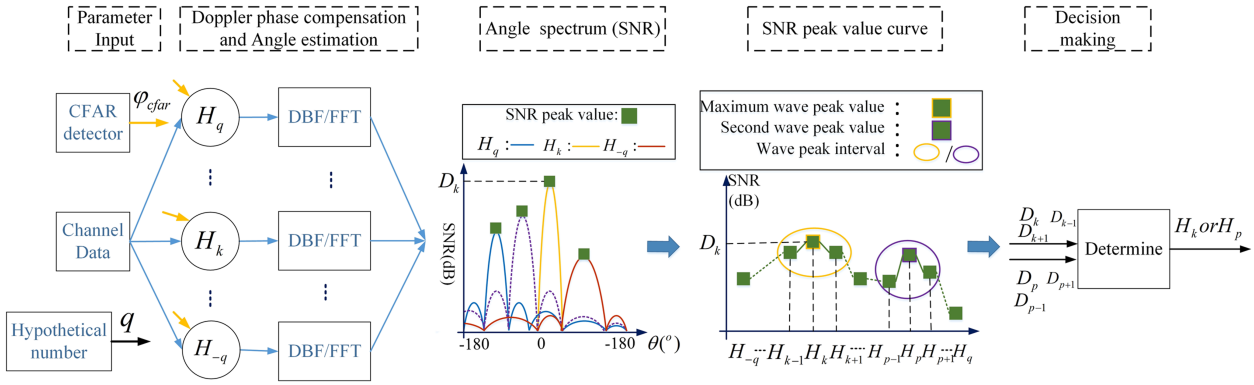

Fig. 5. HPC-SNR algorithm flow.

Step 4 (Decision making): The true Doppler phase of the target is obtained based on the judgment conditions

$$H_{\text{true}}(\phi_{\text{true}}) = \begin{cases} H_k(\phi_k), & \text{if } D_k \gg D_p \\ H_k(\phi_k), & \text{else if } SUM_k \geq SUM_p \\ H_p(\phi_p), & \text{otherwise} \end{cases} \quad (17)$$

where $H_{\text{true}}(\phi_{\text{true}})$ denotes the assumption that corresponds to the real situation (Doppler generated by the true velocity of the target), based on which the true velocity of the target can be obtained.

IV. Simulation and Real Experiment Condition Overview

In this article, MATLAB-based numerical simulations and real experiments based on actual physical platforms and traffic scenarios are implemented to validate the performance of the proposed algorithm and compare it with the HPC-Peak algorithm. In order to make the results of the simulation more credible, as well as to maintain all the experiments uniform and facilitate analysis, all the parameter configurations in the simulation experiments are kept consistent with those of the actual radar system, including the radar antenna array layout, the radar beam parameters, and the signal processing flow. However, the results of the simulation experiments can be considered as the results in an ideal environment since the objects are ideal point targets and the background noise is Gaussian white noise.

First, in our experiments, we verify the performance of the proposed algorithm in terms of both planar imaging and spatial stereo imaging of millimeter-wave radar. Fig. 6 shows two antenna array configurations for simulation and real-world testing, both consisting of 12 TXs and 16 RXs but with different array layouts. In array A [as shown in Fig. 6(a)], most antennas are distributed in the azimuthal dimension resulting in a high directional angular resolution, and thus, the array is used for planar imaging simulation and testing. In array B [as shown in Fig. 6(b)], the antennas are uniformly distributed in the azimuth and pitch dimensions, and thus, the array is used for spatial imaging simulation and testing.

Next, the simulation model and the actual radar configuration parameters are the same, i.e., the radar has the same performance, including distance resolution, speed resolution, angle resolution,

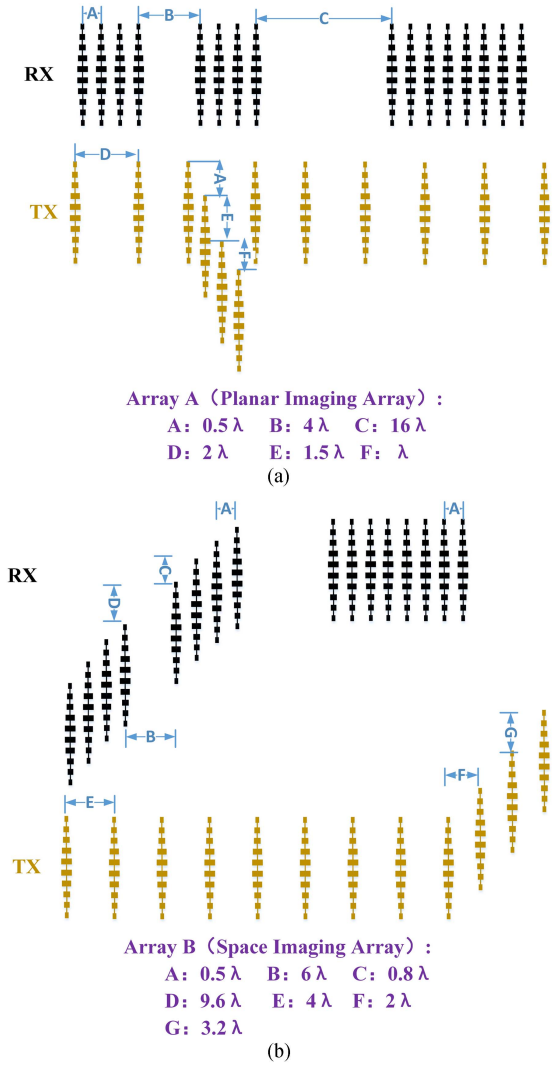

Fig. 6. Antenna array layout of radar systems. (a) Antenna array A for planar imaging. (b) Antenna array B for spatial imaging.

etc. The parameters are shown in Table I. In the table, superscript 1 denotes a planar imaging radar system parameter, and superscript 2 denotes a spatial imaging radar system parameter; a

TABLE I
RADAR SYSTEM PARAMETERS

Item	Parameters	Item	Parameters
Range FFT points	512	Chirp number	64
f_{adc}	20 MHz	B	1.54 GHz
R_{max}	50 m	V_{max}	2.14 m/s
$R_{resolution}$	0.098 m	$V_{resolution}$	0.067 m/s
$A^1_{resolution}$	1.4°	$E^1_{resolution}$	–
$A^2_{resolution}$	1.6°	$E^2_{resolution}$	2.5°
Simulation target	Ideal point targets	Real testing	Vehicles

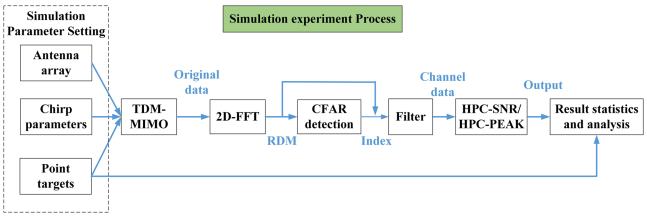

Fig. 7. Radar signal processing process.

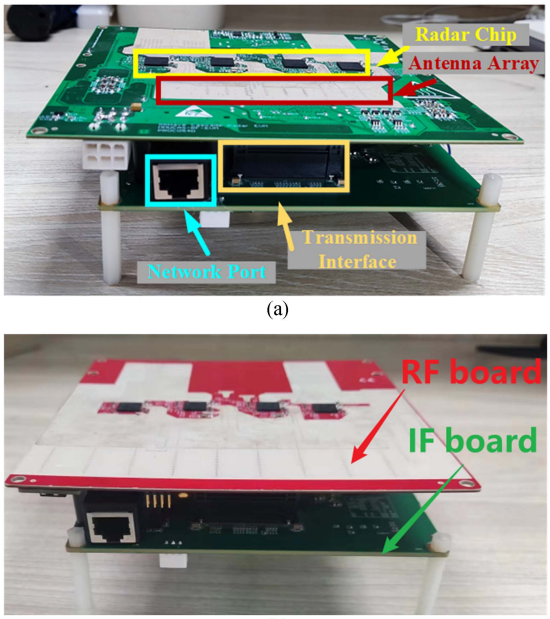

Fig. 8. Radar system physical platform. (a) Planar imaging radar system. (b) Space imaging radar system.

parameter without a superscript indicates that the value is the same in both the radar systems.

Finally, based on the antenna array and radar parameters, we constructed a MATLAB simulation program and the radar system with the same signal processing process for algorithm performance verification. Fig. 7 shows the signal processing flow in the simulation experiment, mainly including the target data setting and raw data acquisition part, the signal processing part, including the proposed algorithm, and the result statistical analysis part. In actual experiments, the radar system platform provides a carrier for implementing the algorithm, as shown in Fig. 8. The radar system consists of a radio frequency (RF) board and an intermediate frequency (IF) board. The RF board based on four radar chips and antenna arrays is used for radar

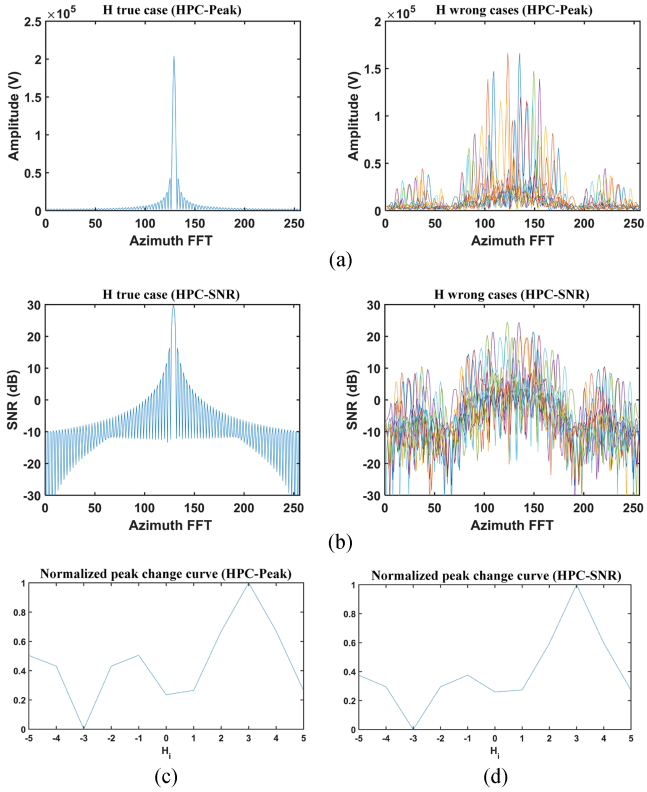

Fig. 9. (a)–(d) Schematic diagram of amplitude or SNR changes under different H conditions in the planar imaging system.

signal transmission, receive, and target raw data acquisition. In the IF board, we use the physical architecture of FPGA+RAM to provide a platform for software development. At the same time, six pieces of DDR memory (two on the FPGA side and four on the RAM side) are used to support the data processing and data flow of the algorithm. The final processing result will be transmitted through the network port for statistics and analysis.

V. NUMERICAL SIMULATIONS AND ANALYSIS

A. Single-Angle Signal Simulation Experiment

Based on two antenna arrays and radar signal processing models, the HPC-SNR algorithm function is implemented for simulation validation and comparison with the HPC-Peak algorithm.

Fig. 9 shows the test results of both the HPC algorithms with the planar imaging antenna array. The peaks of the angular power spectrum and the angular SNR spectrum are highest only when the compensated phase coincides with the Doppler phase produced by the target's actual velocity (H true case), as shown in Fig. 9(a) and (b). The peaks of the angular spectra at each H are extracted to form a peak change curve; then, H corresponding to the highest point of the curve is the correct case, as shown in Fig. 9(c) and (d). Similarly, the same test results are obtained under spatial imaging antenna array, as shown in Fig. 10. Only if the correct phase compensation (H true case) is performed, the target position and the correct number of targets are clearly

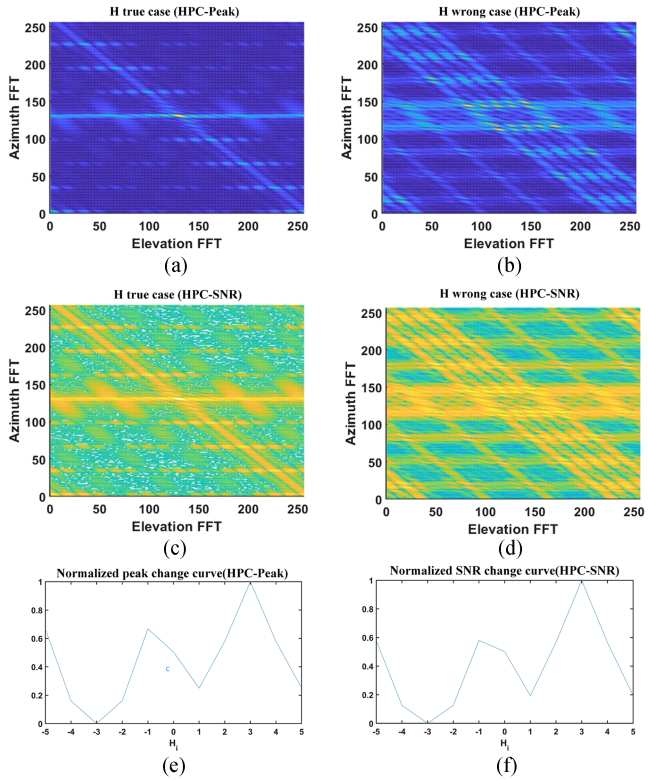

Fig. 10. (a)–(f) Schematic diagram of amplitude or SNR changes under different H conditions in the spatial imaging system.

presented in the target azimuth–pitch angle spectrum or SNR spectrum. The normalized curve shows that the peak or SNR value at the target is the highest at the H true case.

Multiple independent repetitions of the experiment were implemented with the target at different angles, as shown in Fig. 11. Although the target velocity is increasing, the error between the target actual velocity and the estimated velocity value does not exceed 0.6˜m/s, and the error between the target real angle and the estimated angle value does not exceed 0.15°.

Through several repetitive simulation experiments, it can be concluded that our proposed improved algorithm has the ability of velocity ambiguity, can correctly solve for the correct velocity and angle of the target under planar imaging and spatial imaging, and has the same processing cycle as the original algorithm. Moreover, the performance of the proposed HPC-SNR algorithm is similar to that of the HPC-Peak algorithm when there is only a single target or single angle signal in the range–Doppler cell.

B. Multiangle Signal Simulation Experiment

The most significant advantage of HPC-SNR is that when multiple targets are in the same range–Doppler unit, it can stably and correctly give all targets' true speed and angle information, which is needed for traffic imaging applications. Fig. 12 shows the velocity disambiguation performance of HPC-Peak and HPC-SNR algorithms when multiple targets are in the same

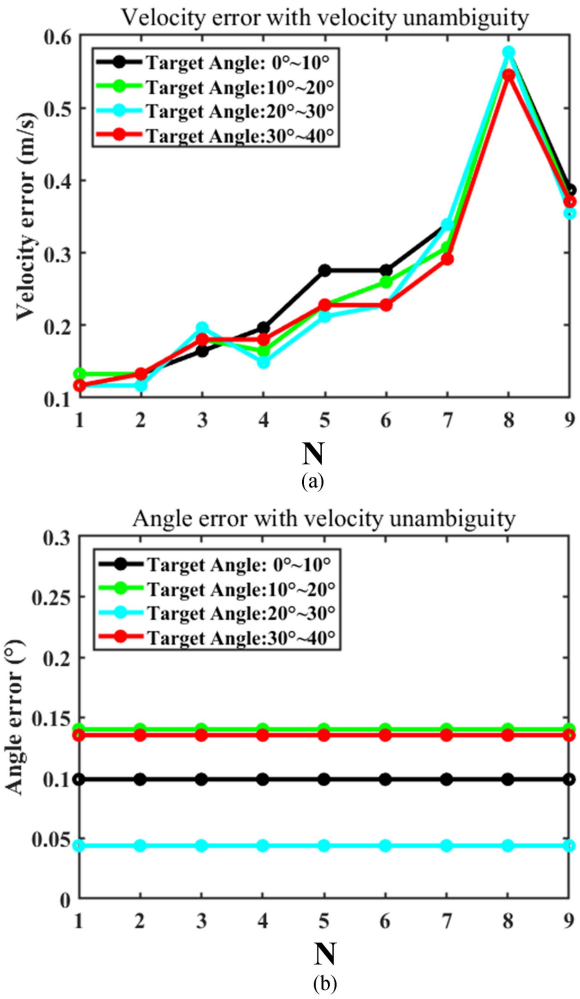

Fig. 11. Functional simulation results of the HPC-SNR algorithm. (a) Velocity estimation error under different maximum unambiguous velocity multipliers (N). (b) Angle estimation error under different maximum unambiguous velocity multipliers (N).

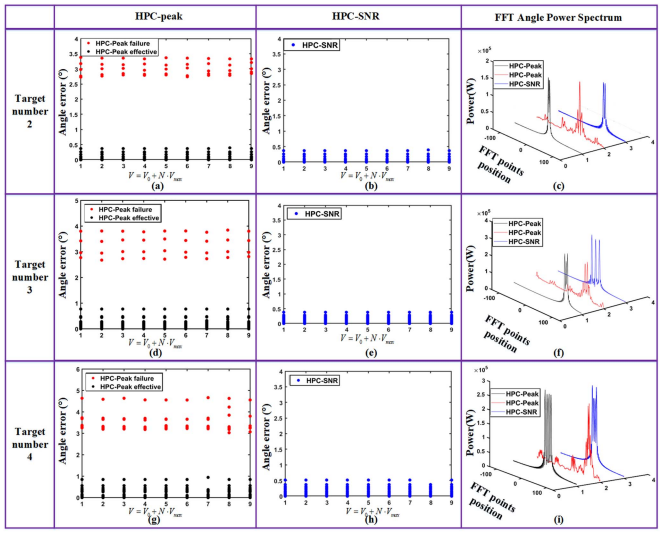

Fig. 12. (a)–(i) Simulation results of the HPC-Peak and the HPC-SNR algorithms with different number of targets.

range–Doppler cell. In the simulation, multiple angle values were randomly selected from $-40°$ to $40°$. Angles with different values are randomly combined to form angle test groups, such as (θ_i, θ_j), $(\theta_i, \theta_j, \theta_p)$ or $(\theta_i, \theta_j, \theta_p, \theta_q)$, where $(\theta_i \neq \theta_j \neq \theta_p \neq \theta_q)$. In addition, the difference between angular values belonging to the same angle test group is larger than the angular resolution of the radar.

We use the error between the estimated angle obtained after velocity compensation and the actual value to measure the algorithm's performance, as shown in Fig. 12(a), (b), (d), (e), (g), and (h). Fig. 12(c), (f), and (i) shows the angular power spectrum waveform after HPC algorithm compensation and FFT operation. The FFT points represent the angle frequency points of the target, i.e., targets at different angles are located at different frequency locations. The number of spectrum peaks represents the number of targets.

It can be seen that some angle groups may make the HPC-Peak algorithm fail when multiobject velocity disambiguation. Once HPC-Peak fails, there will be a large error between the estimation angle of the target and the real one (the maximum error can reach $5°$), as shown by the red dot area in Fig. 12(a), (d), and (g). The number of peaks in the angular power spectrum does not match the true number of targets (as shown in the red angular spectrum waveform in Fig. 12(c), (f), and (i), i.e., the number of targets is misestimated. On the contrary, the HPC-SNR algorithm has always maintained good performance in Doppler compensation. Throughout the experiment, the error between the estimated angle and the actual value does not exceed 0.5°, and the number of peaks of the power spectrum is consistent with the number of actual targets, as shown by the blue dot area and waveform in Fig. 12(b), (e), (h), (c), (f), and (i).

Fig. 13 shows the results of one of the repeated experiments. The parameters of the simulation experiment are: the number of targets is three, the target speed is $v \in (5v_{\max}, 6v_{\max})$, and the target angle is $\theta = [0°, 3°, 6°]$. According to the phase relationship, the correct compensation should be H_3. Fig. 13(a) and (b) shows the detection results of the two HPC algorithms. In the HPC-Peak algorithm, the highest peak point is H_5, so the algorithm cannot get the correct phase compensation value. However, the HPC-SNR algorithm's SNR curve is highest only at H_3 so that the target data can get the correct Doppler phase compensation. The fundamental reason for the HPC-Peak algorithm's failure is that the angular spectrum's power variation is unstable. Fig. 13(c) and (d) shows the angular power spectrum for the H_5 and H_3 cases. In H_3, the angular power spectrum has three clear target peaks, while in H_5, the angular power spectrum has the wrong number of heights and a distorted waveform. However, the value of the highest peak in H_5 is larger than that in H_3 due to the effect of the bottom noise, so the correct result cannot be obtained using the HPC-Peak algorithm. However, the problem can be effectively avoided by utilizing the HPC-SNR algorithm because the magnitude of the SNR is unaffected despite the elevated target peak, as shown in Fig. 13(e) and (f).

Similarly, the same situation occurs in planar arrays. The parameters of the simulation experiment are: the number of targets is four, the target speed is $v \in (5v_{\max}, 6v_{\max})$, the target azimuth angle is $[0.6°, 3.1°, 5.6°, 8.1°]$, and the target elevation angle is

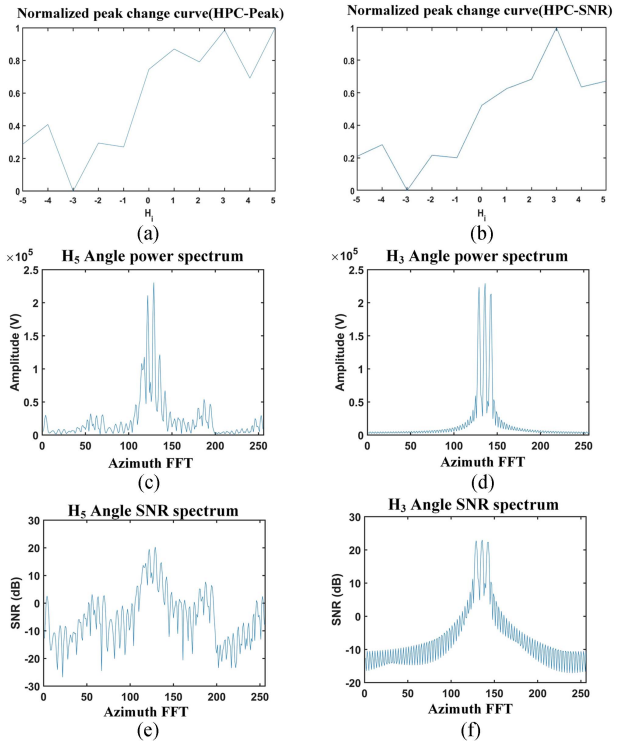

Fig. 13. (a)–(f) Comparison and analysis of algorithmic failure results in planar imaging.

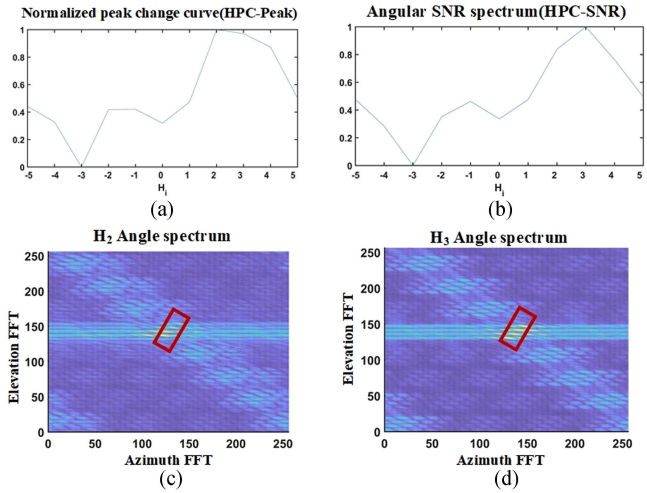

Fig. 14. (a)–(d) Comparison and analysis of algorithmic failure results in spatial imaging.

$[0.6°, 3.1°, 5.6°, 8.1°]$. Utilizing the HPC-Peak algorithm does not give the correct compensation results, and there are only three targets in the azimuth–pitch angle power spectrum [as shown in Fig. 14(a) and (c)]. However, the correct target Doppler compensation value and the number of targets can be obtained using the HPC-SNR algorithm [as shown in Fig. 14(b) and (d)].

C. Discussion and Summary Under Simulation Experiments

Through the experiment, the following conclusions can be obtained.

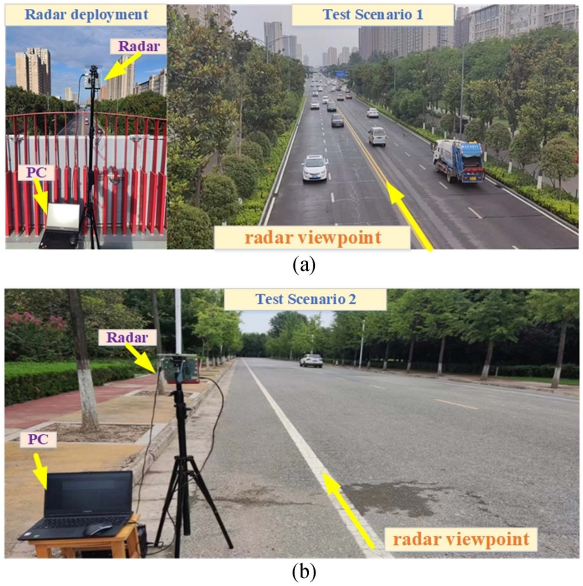

Fig. 15. Traffic test scenarios. (a) Planar imaging traffic scene. (b) Spatial imaging traffic scene.

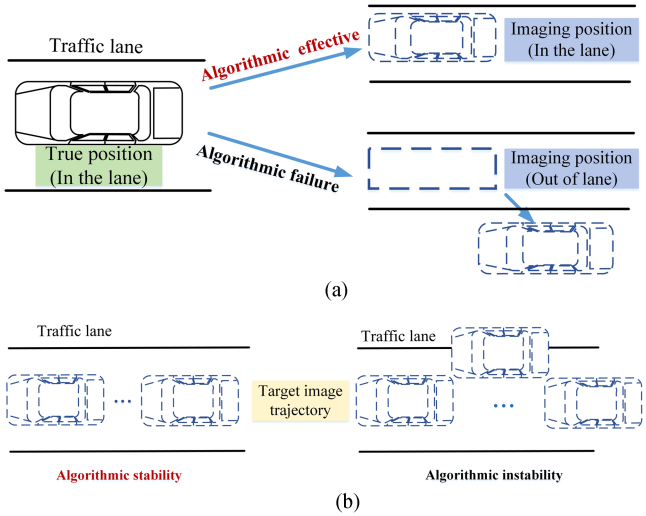

Fig. 16. Schematic diagram of algorithm performance evaluation methods. (a) Algorithm performance evaluation method based on point cloud image location. (b) Algorithm performance evaluation method based on point cloud image location trajectory.

1) The proposed improvement points do not affect the algorithm's ability to deal with speed ambiguity. In particular, the performance of the HPC-SNR and HPC-Peak algorithms is similar under single-angle signal or single-target conditions.
2) When multiple targets are in the same range–Doppler cell, the performance of the HPC-Peak algorithm is unstable. Once the algorithm fails, there is a large error between the estimated angle and the actual value, and the number of targets is incorrectly estimated. However, the HPC-SNR algorithm performs well in multiobject situations, and the angular power spectrum can correctly reflect the number of targets, which is crucial for millimeter-wave radar imaging applications.
3) The angle estimation error of the HPC-SNR algorithm is smaller under multiangle signals, even when both the algorithms are valid.
4) The proposed algorithm is independent of the antenna array. It is suitable for both planar imaging under the radar 1-D array and spatial imaging under the radar 2-D array.

VI. Practical Scenario Experiments and Analysis

A. Test Scenario and Evaluation Method Definition

We verify and compare the performance of the proposed algorithm on real roads by testing on vehicles traveling at different speeds, in different directions, and on different lanes. Fig. 15 illustrates two algorithmic test scenarios. In scenario A, the radar with antenna array A is set up on an overpass to perform planar images of vehicles in the lane in a top-down view, as shown in Fig. 15(a). In scenario B, the radar with antenna array B is set up on the side of the roadway to perform the spatial imaging of vehicles on the road from a side-view perspective, as shown in Fig. 15(b). The radar center is taken as the coordinate origin, the direction of the radar beam (parallel to the lane direction) as the Y-axis, and the perpendicular to the direction of the radar beam (perpendicular to the direction of the lane) as the X-axis. The target speed away from the radar is defined as positive speed, otherwise negative speed. To facilitate the experimental comparison with the simulation results, the parameters of the two radar systems in the actual experiment are the same as in Table I.

It is inconvenient to accurately measure the speed of vehicles traveling on the road in a practical test. Therefore, to better characterize and compare the performance of the algorithms, we define an evaluation method that is easy to statistically and operationally evaluate before testing. According to the relationship between target velocity error and angle, it can be seen that the wrong velocity compensation will make the angle estimation fail, which makes the target's position in space necessarily deviate from the actual position. The trajectory of a usually traveling vehicle is bound to coincide with the lane. Therefore, in this article, we utilize the locations and trajectories of vehicle point cloud images formed by radar imaging or continuous imaging operations to evaluate the performance of the algorithms. As shown in Fig. 16(a), if the position of the vehicle's point cloud image should be the same as the actual lane where the vehicle is located, then the algorithm is effective; otherwise, the algorithm fails. At the same time, we use the target's point cloud image trajectory to assess the algorithm's stability. As shown in Fig. 16(b), if the trajectory formed by the target's point cloud image overlaps with the lane during continuous imaging, then the algorithm has good stability. If the trajectory is discrete and fluctuating, the algorithm has poor stability. Similarly, the algorithm accuracy can also be evaluated by fitting the center of the target trajectory.

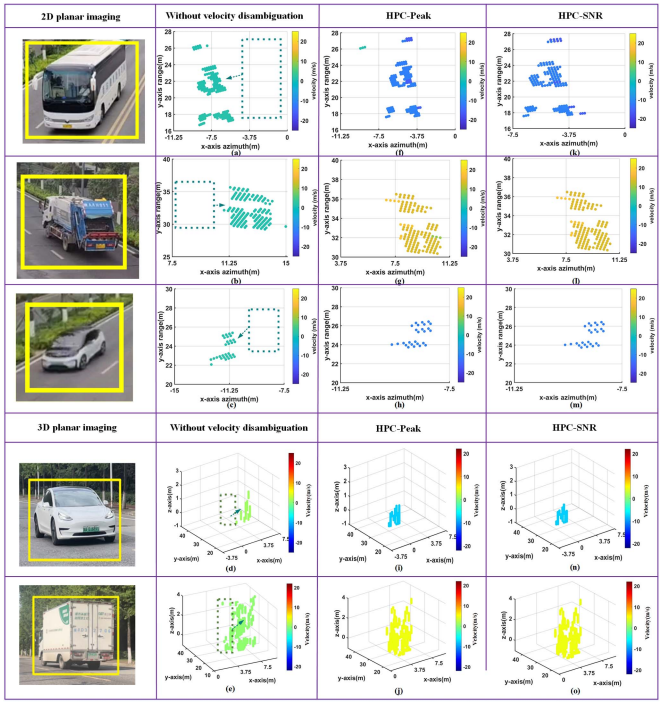

Fig. 17. (a)–(o) Functional testing of speed disambiguation algorithms in field scenarios.

B. Functional Verification

Based on two types of millimeter-wave radar platforms and real targets, the importance of velocity ambiguity resolution algorithms is demonstrated in both planar imaging and stereoscopic imaging, as shown in Fig. 17. Fig. 17(a)–(e) verifies in a real data way that the Doppler generated by the target speed affects the correctness of the radar angle estimation. When the target speed exceeds the radar maximum detectable speed, the point cloud image position of the vehicle obviously deviates from the original lane if the speed disambiguation process is not taken. The greater the velocity, the more obvious the point cloud image position deviation. When the speed disambiguation algorithm is applied, the radar's point cloud imaging correctly reflects the actual position and shape of the vehicle, i.e., the vehicle's point cloud image is always in the correct lane position regardless of the speed and direction of travel.

As demonstrated in Fig. 17, our improvements to the HPC-Peak algorithm do not affect the algorithm's ability to solve the speed ambiguity. The proposed HPC-SNR can improve the radar's maximum detectable speed range, and the improved range is basically consistent with the theory. Under the radar system in this article, the radar-detectable target speed has been higher than the radar maximum unambiguous speed [as shown in Fig. 17(f) and (o)], and the maximum speed can be up to 18˜m/s [e.g., Fig. 17(g) and (i)]. In addition, the proposed algorithm is applicable in both the planar and spatial imaging applications.

C. Performance Verification

We evaluate the algorithm's stability and practical application effectiveness through the trajectories formed by continuous

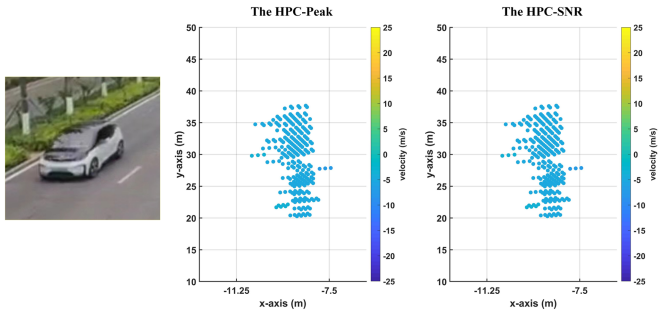

Fig. 18. Small vehicle planar point cloud image trajectory comparison and analysis.

target point cloud images. First, since the maximum detection range of the radar system used in the TDM-MIMO mode is 50 m, the results of the target point cloud image in the 20–40 m range are selected for the experiment to be counted and analyzed. On the one hand, choosing the middle range allows the vehicle to always be within the effective imaging range of the radar. On the other hand, when the target is too close to the radar, strong reflections from the target can cause the point cloud image to extend. When the target is too far away from the radar, the weak reflection of the target's energy results in a sparse point cloud. All these affect the statistics, and analysis of the radar point cloud imaging results should be avoided. Next, the target point cloud image is obtained through radar system reception signals and signal processing with the HPC algorithm, and multiple frame images are aggregated to form the target point cloud trajectory. Finally, the performance and practicality of the algorithm are evaluated by analyzing the point cloud trajectory, including trajectory position, trajectory fluctuation size, target velocity consistency, and the number of abnormal point cloud images.

Figs. 18–21 show the effectiveness of the proposed HPC-SNR algorithm in continuous planar imaging and continuous spatial imaging applications of vehicles and compare it with the original HPC-Peak algorithm. We mark the parts where the results of the two algorithms differ with red boxes or circles and show the point cloud image of that frame independently for easy comparison. At the same time, some imaging frames that are correct for both the algorithms are marked with purple boxes.

Figs. 18 and 19 show the imaging results of the planar imaging radar at a top-view angle. When the object of radar planar imaging is a small vehicle (as shown in Fig. 18), the imaging results obtained by the HPC-SNR algorithm and the HPC-Peak algorithm are almost the same, both for the vehicle point cloud trajectory formed by continuous imaging and for the target point cloud image in a single frame. The point cloud image trajectory is consistent with the actual trajectory of the target. According to statistics, in planar imaging experiments on small vehicles, the proportion of abnormal frames in the HPC-SNR algorithm is 2.5%. The proportion of abnormal frames in the HPC-Peak algorithm is 3.5%.

However, as the size of the vehicle target increases, points with abnormal positions and velocities appear in the target point cloud trajectory, which makes the point cloud trajectory discrete. Compared to the HPC-SNR, there are more abnormal points in

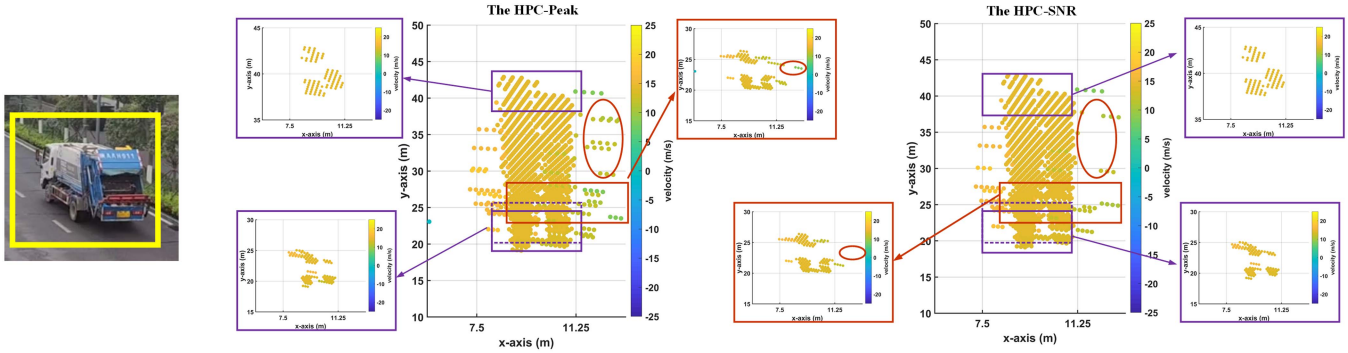

Fig. 19. Large vehicle planar point cloud image trajectory comparison and analysis.

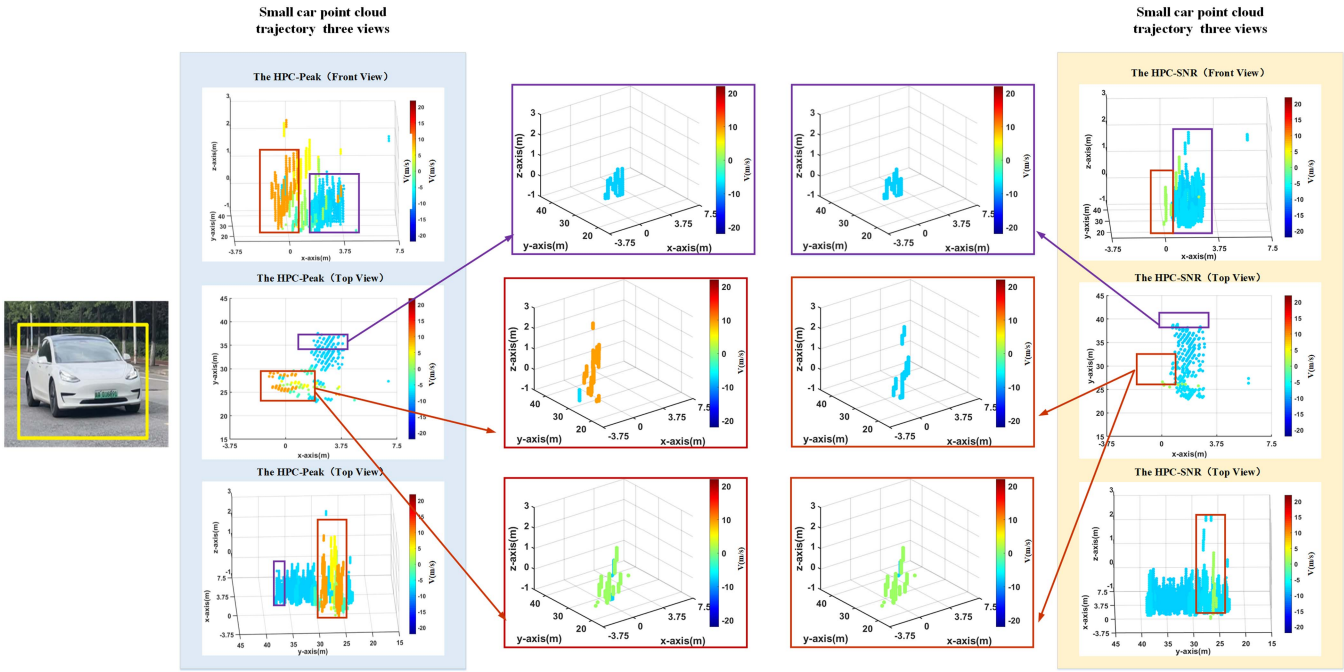

Fig. 20. Small vehicle spatial point cloud image trajectory comparison and analysis.

the results of the HPC-Peak algorithm, as shown in the red-circled area in Fig. 19. When we show the imaging results of one of the frames with discrepancies separately (as shown in the red box in Fig. 19) and compare them, we can see that the vehicle point clouds are more concentrated, and the velocities between the point clouds are approximately the same (with the same orange velocity points) in the imaging results of the proposed HPC-SNR algorithm. In contrast, in the imaging results of the HPC-Peak algorithm, there are some points with completely wrong velocities (green velocity points), impacting the imaging quality. According to statistics, in planar imaging experiments on large vehicles, the proportion of abnormal frames in the HPC-SNR algorithm is 8.5%. The proportion of abnormal frames in the HPC-Peak algorithm is 13.5%.

Figs. 20 and 21 show the imaging results of spatial imaging radar in roadside scenes. For the point cloud trajectories formed by the same target, we present them in three ways: front view, side view, and top view for easy observation. Fig. 20 shows the continuous spatial imaging results of the spatial imaging radar system for small vehicles. Although the objects imaged by the radar system are both small vehicles, there are large differences between the trajectory images formed by the two algorithms. The HPC-SNR algorithm remains effective almost continuously throughout the imaging section, and it can correctly solve the target's actual velocity so that the target point cloud image is in the correct position, and the point cloud trajectory is consistent with the target's actual trajectory. However, the performance of the HPC-Peak algorithm decreases significantly. When the vehicle is far from the radar, the performance of the HPC-Peak algorithm remains the same as that of the HPC-SNR, but as the distance between the car and the radar decreases, the HPC-Peak begins to fail. Compared to the results of planar imaging, the error in spatial imaging is more significant when HPC-Peak fails. The radar completely misestimates the vehicle's speed

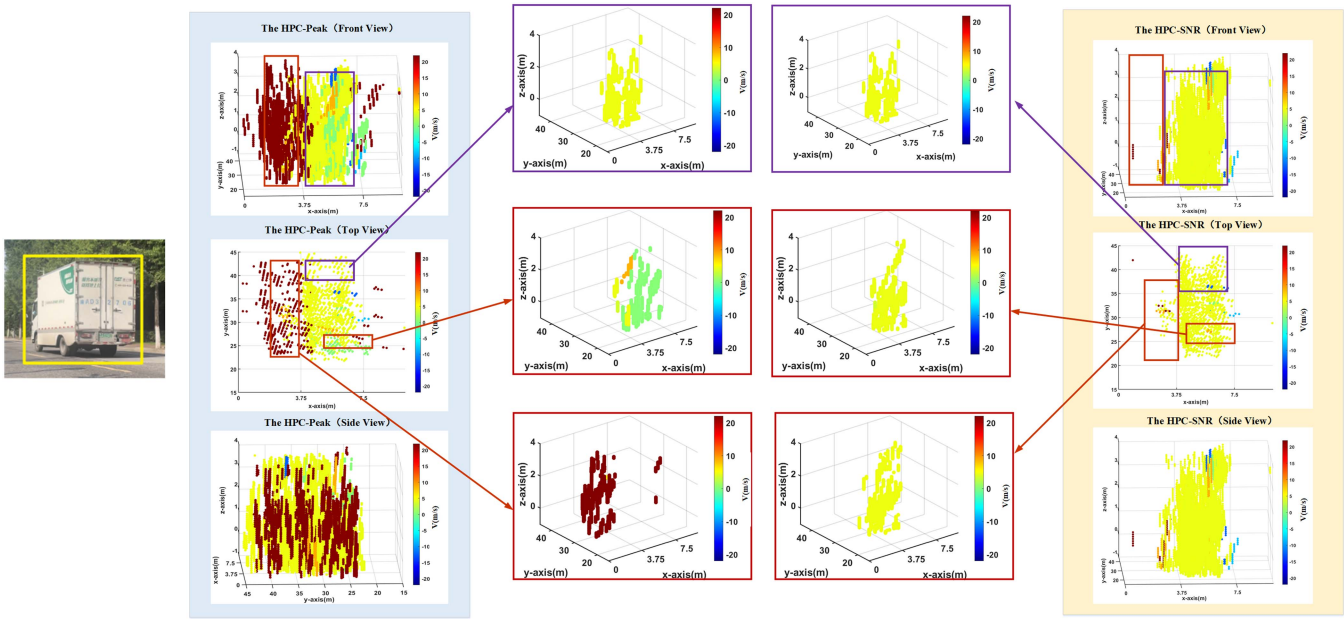

Fig. 21. Large vehicle spatial point cloud image trajectory comparison and analysis.

and direction of travel, and the location of the point cloud image is far from the correct lane. According to statistics, in spatial imaging experiments on small vehicles, the proportion of abnormal frames in the HPC-SNR algorithm is 10.5%. The proportion of abnormal frames in the HPC-Peak algorithm is 26.5%.

Fig. 21 shows the results of continuous imaging of a large vehicle by the spatial imaging radar. The performance of the HPC-Peak algorithm deteriorates further, and the algorithm suffers from failures even when the target is far from the radar. For the HPC-SNR algorithm, the overall results are significantly better than the HPC-Peak algorithm, even though there are some anomalies in the point cloud image. According to statistics, in spatial imaging experiments on large vehicles, the proportion of abnormal frames in the HPC-SNR algorithm is 18.5%. The proportion of abnormal frames in the HPC-Peak algorithm is 55.5%.

D. Discussion and Summary Under Practical Experiments

We analyzed the results of the point cloud images that appeared in the actual experiments, and there were four cases.

1) When both the HPC-Peak and HPC-SNR algorithms are effective, the wave peak value in the correct H case is the highest and much larger than the other positions both in the normalized angular power spectrum curve and normalized SNR curve, as shown in case 1 in Fig. 22.
2) The advantage of the proposed HPC-SNR algorithm is that it can still implement the correct velocity estimation stably and efficiently when there are multiple targets or angular information in the same range–Doppler cell. In practice, increasing target size increases the probability that different parts of the target itself fall in the same distance Doppler region. Compared to planar imaging radar systems, spatial radar systems can form more point clouds due to the planar array antennas allowing the radar to detect target height information, further increasing the probability of multiple angular information (or multiple targets) within the same range–Doppler cell. Multiple angular information can exist in the same distance Doppler cell when imaging large vehicles compared to small ones, especially in spatial imaging. At this point, using angular spectral peaks for decision making is unreliable since the angular signals interfere with each other. As shown

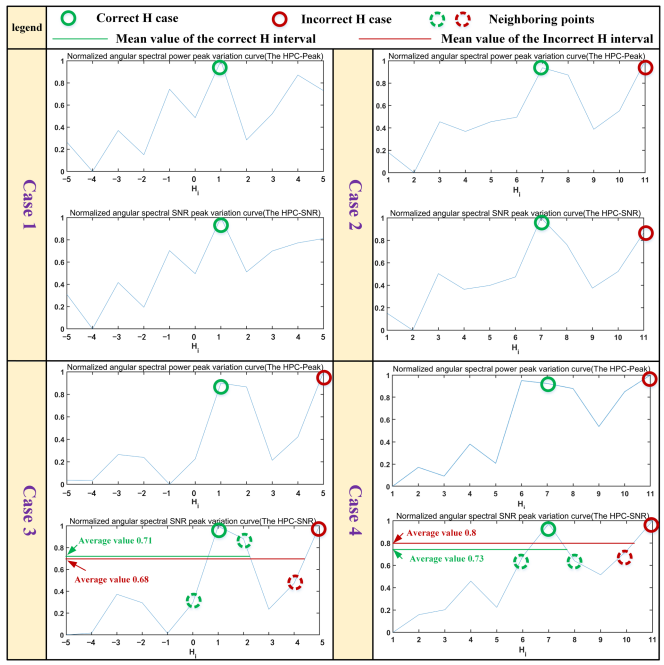

Fig. 22. Four cases in the actual test.

in case 2 in Fig. 22, the peak at the true H position in the normalized angular power spectrum curve is not the highest, at which point the HPC-Peak algorithm fails. The more angular information there is, the larger the algorithm error, which is consistent with the previous numerical simulation results (shown in Fig. 12). However, the HPC-SNR algorithm can remain effective because the bottom noise is less affected by the SNR. Therefore, the advantage of the HPC-SNR algorithm in experiments with large vehicles is more obvious.

3) Relying only on the highest SNR value for decision making is unstable. As in case 3 in Fig. 22, the actual experiment also shows that the location of the maximum SNR value in the normalized SNR curve is not the actual H location due to the nonideal environment, which cannot be found in the simulation experiment. To solve this problem, when the value of the highest wave crest is similar to that of the second-highest wave crest, the mean value of the waveform interval is used for the secondary decision. Obviously, the mean value of the true H position interval is higher than the mean value of the false H position interval, since the higher the phase compensation accuracy, the higher the angular power spectrum is maximized.
4) However, adding the wave interval mean judgment does not completely solve all the problems. As in case 4 in Fig. 22, there exists an SNR curve in which the highest point is not the correct H position, and the mean value of the wrong H interval is also larger than the mean value of the correct H position interval. The HPC-SNR algorithm will fail at this point, corresponding to the experiment's outlier part. Fortunately, the number of anomalies and the percentage of occurrence probability are very small and have a small impact on imaging.

The overall planar and spatial imaging experiments show that the proposed HPC-SNR algorithm is significantly better than the HPC-Peak algorithm and is more suitable for the imaging applications of MIMO radar systems, which is consistent with the simulation conclusions. The HPC-SNR algorithm maintains a good velocity disambiguation capability, which is not the case with the HPC-Peak algorithm, despite the fact that there are multiple angular signals in the same range–Doppler cell due to the increase of the target size or the increase of the angular dimensional information of the radar system. The two radar systems with different antenna arrays also show that the proposed algorithm is not limited by the antenna arrays.

VII. Conclusion

This article proposes a velocity estimation algorithm based on improved hypothetical phase compensation (HPC-SNR) for TDM-MIMO radar traffic target imaging. Numerical simulations and real experiments are also provided and analyzed. The algorithm has the following characteristics and advantages.

1) The HPC-SNR algorithm still retains the advantages of the original HPC algorithm, i.e., in a single data frame (without changing the radar transmission waveform), the maximum detectable speed of the radar is increased by M times (when M is an odd number), where M is the number of transmission antennas.
2) Compared to the original HPC algorithm, the proposed HPC-SNR algorithm is more accurate and stable, especially when there are multiple targets or angle signals in the same range–Doppler cell, and is also more suitable for MIMO radar imaging applications.
3) Experiments have shown that the proposed algorithm is suitable for both radar planar imaging and spatial stereo imaging, i.e., it is not affected by the antenna array layout.

However, there are also failures of HPC-SNR, which can affect the imaging quality. In the future, we would like to correct or remove outliers in the imaging traces by using a joint clustering algorithm.

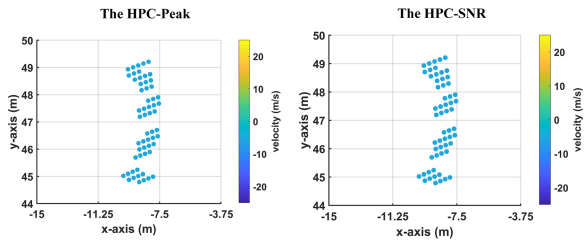

Fig. 23. Small vehicle planar point cloud image trajectory in long range.

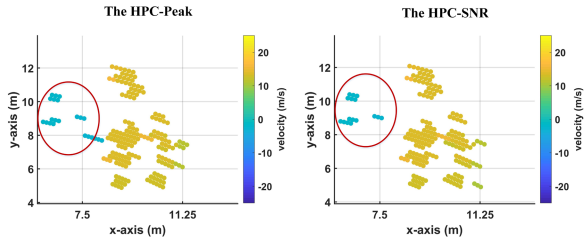

Fig. 24. Large vehicle planar point cloud image trajectory in close range.

Appendix
Explanation of Target Point Cloud Images in Close Range and Long Range

Here, we add two additional experiments (shown in Figs. 23 and 24) to illustrate two main points: first, the proposed algorithm is not limited by distance and is applicable throughout the detection range of the radar system; second, the core purpose of choosing the intermediate distance segment of the radar system in the experiments in the main text is to make the target present a better point-cloud image to facilitate the observation and comparison of the algorithm performance.

When the target is too far from the radar, the target point cloud density presented by the radar system will decrease due to the influence of radar angular resolution and target reflection intensity, leading to sparse point cloud trajectories, especially for small-volume targets. The target in Fig. 23 is the same as the target in Fig. 19, but due to distance differences, the trajectory's density and area vary greatly. Obviously, the trajectory of the target point cloud at a long distance is difficult to observe and analyze. However, the proposed HPC-SNR algorithm remains effective.

When the target is too close to the radar, the strong reflection from the target causes the point cloud image to expand as well as out multipath effect, and the occlusion of the target itself causes the target image to be incomplete, especially for large volume targets. The target in Fig. 24 is the same as the one in Fig. 20, but the target's proximity to the radar leads to multipath effects (as shown by the red circle in Fig. 24) and incompleteness in the point cloud image. Obviously, these additional interferences are not conducive to the observation and comparison of the algorithm performance and are not the focus of this article. Therefore, the point cloud trajectories of targets that are particularly close to the radar are not considered in the experiments in the main text. However, the proposed HPC-SNR algorithm is still effective in close-range imaging.

Improving the radar point cloud density at long distances and reducing the scattering of close-range targets is a hot research topic in radar imaging. These phenomena can occur in both the planar and spatial imaging radar systems, but these are not the focus of this article and do not affect the application of the proposed HPC-SNR algorithm.

REFERENCES

[1] A. Prabhakara et al., "High resolution point clouds from mmWave radar," in *Proc. IEEE Int. Conf. Robot. Automat. (ICRA)*, 2023, pp. 4135–4142, doi: 10.1109/ICRA48891.2023.10161429.

[2] H. Liu, N. Li, D. Guan, and L. Rai, "Data feature analysis of non-scanning multi target millimeter-wave radar in traffic flow detection applications," *Sensors*, vol. 18, no. 9, 2018, Art. no. 2756.

[3] E. Klinefelter and J. A. Nanzer, "Automotive velocity sensing using millimeter-wave interferometric radar," *IEEE Trans. Microw. Theory Techn.*, vol. 69, no. 1, pp. 1096–1104, Jan. 2021.

[4] X. Li, X. Wang, Q. Yang, and S. Fu, "Signal processing for TDM MIMO FMCW millimeter-wave radar sensors," *IEEE Access*, vol. 9, pp. 167959–167971, 2021.

[5] B. Liu, "Orthogonal discrete frequency-coding waveform set design with minimized autocorrelation sidelobes," *IEEE Trans. Aerosp. Electron. Syst.*, vol. 45, no. 4, pp. 1650–1657, Oct. 2009.

[6] H. Sun, F. Brigui, and M. Lesturgie, "Analysis and comparison of MIMO radar waveforms," in *Proc. Int. Radar Conf.*, 2014, pp. 1–6.

[7] H. Cui, J. Wu, J. Zhang, G. Chowdhary, and W. R. Norris, "3D detection and tracking for on-road vehicles with a monovision camera and dual low-cost 4D mmWave radars," in *Proc. IEEE Int. Intell. Transp. Syst. Conf.*, 2021, pp. 2931–2937.

[8] G. Li et al., "Pioneer study on near-range sensing with 4D MIMO-FMCW automotive radars," in *Proc. 20th Int. Radar Symp.*, 2019, pp. 1–10.

[9] T.-Y. Lee, V. Skvortsov, M.-S. Kim, S.-H. Han, and M.-H. Ka, "Application of w-band FMCW radar for road curvature estimation in poor visibility conditions," *IEEE Sens. J.*, vol. 18, no. 13, pp. 5300–5312, Jul. 2018.

[10] S. M. Sabery, A. Bystrov, P. Gardner, A. Stroescu, and M. Gashinova, "Road surface classification based on radar imaging using convolutional neural network," *IEEE Sens. J.*, vol. 21, no. 17, pp. 18725–18732, Sep. 2021.

[11] M. Lei, D. Yang, and X. Weng, "Integrated sensor fusion based on 4D MIMO radar and camera: A solution for connected vehicle applications," *IEEE Veh. Technol. Mag.*, vol. 17, no. 4, pp. 38–46, Dec. 2022.

[12] M. Elbeialy, S. You, B. J. Jeong, and Y. Kim, "Target classification using frontal images measured by 77 GHz FMCW radar through DCNN," *Appl. Sci.*, vol. 12, no. 20, 2022, Art. no. 10264.

[13] X. Huang, H. Wang, G. Huang, and J. Luo, "Doppler shift detection based on Chinese remainder theorem and spectrum correction," in *Proc. IEEE 23rd Int. Conf. Digit. Signal Process.*, 2018, pp. 1–5.

[14] M. Li and M. Li, "A high efficiency algorithm of PD radar for range ambiguity resolution based on the one-dimension method," *Electron. Inf. Warfare Technol.*, vol. 25, no. 5, pp. 22–25, 2010.

[15] S. Zhang, "An improved method of range ambiguity resolution using look-up table," *Inf. Res.*, vol. 41, no. 2, pp. 23–26, 2015.

[16] X. Hu, Y. Li, M. Lu, Y. Wang, and X. Yang, "A multi-carrier-frequency random-transmission chirp sequence for TDM MIMO automotive radar," *IEEE Trans. Veh. Technol.*, vol. 68, no. 4, pp. 3672–3685, Apr. 2019.

[17] X.-G. Xia, "Doppler ambiguity resolution using optimal multiple pulse repetition frequencies," *IEEE Trans. Aerosp. Electron. Syst.*, vol. 35, no. 1, pp. 371–379, Jan. 1999.

[18] X.-G. Xia and G. Wang, "Phase unwrapping and a robust Chinese remainder theorem," *IEEE Signal Process. Lett.*, vol. 14, no. 4, pp. 247–250, Apr. 2007.

[19] W. Wang and X.-G. Xia, "A closed-form robust Chinese remainder theorem and its performance analysis," *IEEE Trans. Signal Process.*, vol. 58, no. 11, pp. 5655–5666, Nov. 2010.

[20] I. Bilik et al., "Automotive MIMO radar for urban environments," in *Proc. IEEE Radar Conf.*, 2016, pp. 1–6.

[21] C. Zhang, M. Cao, Y. Li, Y. Gong, and Y. Huang, "Velocity ambiguity resolution for wideband automotive millimeter wave radar: A carrier frequency multiplexing framework," *J. Electromagn. Waves Appl.*, vol. 34, no. 3, pp. 375–389, 2020.

[22] C. M. Schmid, R. Feger, C. Pfeffer, and A. Stelzer, "Motion compensation and efficient array design for TDMA FMCW MIMO radar systems," in *Proc. 6th Eur. Conf. Antennas Propag.*, 2012, pp. 1746–1750.

[23] M. Dikshtein, O. Longman, S. Villeval, and I. Bilik, "Automotive radar maximum unambiguous velocity extension via high-order phase components," *IEEE Trans. Aerosp. Electron. Syst.*, vol. 58, no. 1, pp. 743–751, Feb. 2022.

[24] H. A. Gonzalez, C. Liu, B. Vogginger, and C. G. Mayr, "Doppler ambiguity resolution for binary-phase-modulated MIMO FMCW radars," in *Proc. Int. Radar Conf.*, 2019, pp. 1–6.

[25] C. Liu, H. A. Gonzalez, B. Vogginger, and C. G. Mayr, "Phase-based Doppler disambiguation in TDM and BPM MIMO FMCW radars," in *Proc. IEEE Radio Wireless Symp.*, 2021, pp. 87–90.

Bo Yang (Student Member, IEEE) received the B.S. degree in telecommunications engineering from the Civil Aviation University of China, Tianjin, China, in 2018. He is currently working toward the Ph.D. degree in navigation guidance and control with Xidian University, Xi'an, China.

Currently, he is undertaking and researching some scientific research projects on millimeter wave radar imaging algorithm and their application in transportation. His research interests include radar detection and radar imaging and their applications.

Siqi Liu (Student Member, IEEE) received the B.S. degree in mechanical and electrical engineering in 2021 from Xidian University, Xi'an, China, where she is currently working toward the master's degree in control science and engineering.

Currently, she is undertaking and researching some scientific research projects on millimeter-wave radar imaging algorithms and point cloud condensation algorithms. Her research interests include radar data processing and 4-D millimeter wave radar imaging.

Hua Zhang received the Ph.D. degree in circuits and systems from Xidian University, Xi'an, China, in 2011 .

In 2019, he became a Professor with the School of Aerospace Science and Technology, Xidian University, where he is the Director of the Department of Guidance, Navigation and Control. In recent years, he has undertaken and completed more than 20 major national and ministerial scientific research projects on radar system design, millimeter-wave radar navigation, and protection technology. He has edited three textbooks and authored or coauthored more than 40 SCI papers. He holds more than 25 parents. He is a peer reviewer of many significant journals, such as IEEE JOURNAL OF QUANTUM ELECTRONICS and *IET Radar Sonar and Navigation*. His research interests include radar imaging detection and application, quantum timing positioning technology, time-varying astronomical signal processing, and navigation mechanisms.

Yongjun Zhou received the M.D. degree in communications engineering from Shanghai Jiao Tong University, Shanghai, China, in 2010 .

He is currently a Senior Engineer with the Science and Technology on Near-Surface Detection Laboratory, Wuxi, China. His research interests include Radar detection, near-ground target detection technology, and ammunition smart fuze technology.